JOURNAL OF AIRCRAFT
Vol. 45, No. 3, May–June 2008

Structured and Unstructured Navier–Stokes Solvers for the Third Drag Prediction Workshop

Edward N. Tinoco* and Venkat Venkatakrishnan†
The Boeing Company, Seattle, Washington 98124
and
Chad Winkler‡ and Mori Mani§
The Boeing Company, St. Louis, Missouri 93301

DOI: 10.2514/1.30593

Drag predictions of the DLR-F6 wing body, with and without the FX2B fairing, are demonstrated using both structured and unstructured grid solvers. The ability to accurately predict incremental drag is key to drag-based design and optimization. The focus of this study was to demonstrate drag and grid convergence on the two configurations. Analyses of the F6 configurations were based on the structured Navier–Stokes code, CFL3D, and on two unstructured Navier–Stokes codes, BCFD and CFD++. Drag and grid convergence characteristics, drag polars, and pressure distribution for the configurations are presented. Results illustrate the use of a mature, structured-grid generator and solver compared to the use of two new-technology, unstructured grid generators and solvers.

Nomenclature

C_D	=	drag coefficient
C_L	=	lift coefficient
C_M	=	pitching moment coefficient
C_P	=	pressure coefficient
N	=	number of grid cells
Re	=	Reynolds number based on mean aerodynamic chord
X/C	=	wing chord fraction
α	=	angle of attack

I. Introduction

THE effective use of computational fluid dynamics (CFD) is a key ingredient in the successful design of modern aircraft configurations. The purpose of CFD use in industry is to produce a better product. Toward this end, design engineers use CFD when they believe it will lead to a better product within the allotted budget of time, money, and effort. The resulting application of CFD has revolutionized aerodynamic design [1–3].

Whereas modern CFD methods have proved reliable in correctly predicting pressure distributions, most design decisions are based on forces and moments. Design trades require credible force and moment values. As a result of many improvements in these computations over the last decade, CFD drag predictions are increasingly being used in the preliminary design through advanced phases of aircraft development [4–6].

Common wing design practice has been to design the wing shape so that it gives a desired pressure distribution. The choice of pressure distribution is largely based on the designer's experience, 2-D CFD analysis or test data, and other 3-D designs. For the most part, CFD code acceptance was based on the code's ability to predict surface pressure distribution, including rooftop pressure level, shock location and strength, and postshock recovery on a wing. Choosing the "best" prescribed pressure distribution for a wing of unusual planform—with multi-engines, realistic manufacturing constraints, and the ability to efficiently operate over a variety of flight conditions—is more art than science. A better approach to wing design is to design to drag [3], which requires being able to calculate drag accurately. A valid assessment of a code's ability to compute drag of a typical transport configuration is not trivial. Such assessments are usually based on comparing computational results with experimental wind-tunnel test data. Such correlations should be based on a large set of data, along with a good understanding of both the test and the computation, in order to bound CFD uncertainties and limit their impact on design decisions [7].

Accurate drag prediction, or at least accurate incremental drag prediction between similar configurations, is essential to successful use. CFD drag assessment is an ongoing endeavor, addressing new codes and test data that may be relevant to the latest project of interest. The 3rd AIAA CFD Drag Prediction Workshop (DPW3) provided another opportunity for CFD drag assessment [8–10]. The workshop focused on drag and grid convergence characteristics and drag increment prediction accuracy of the DLR-F6 transport model, with and without the FX2B fairing, and a pair of simple trapezoidal wings. The workshop provided an impartial forum for evaluating the effectiveness of existing computer codes and modeling techniques using Navier–Stokes solvers for participants from North America, Europe, and Asia representing government agencies, academia, and industry. This paper focuses only on the DLR-F6 results. Results for the wing-alone configurations can be found on the DPW Web site [10].

II. Geometry

The DLR-F6 configuration represents a twin-engine, wide body aircraft of the Airbus type; it was also the subject of the 2nd AIAA CFD Drag Prediction Workshop held in June 2003. The DLR-F6 configuration was designed for cruise Mach = 0.75 at $C_L = 0.50$. It was originally tested at the ONERA S2M wind tunnel, at a Reynolds number of 3×10^6 based on the mean aerodynamic chord. The basic DLR-F6 model is shown in Fig. 1. The nacelle and pylon were not considered in the third AIAA DPW. For that workshop, a wing-body fairing was designed to eliminate the side-of-body separation near the wing upper-surface trailing edge [11]. The FX2B wing-body fairing is illustrated in Fig. 2. It is planned that the basic wing-body model and the model with the addition of the FX2B fairing will be the

Presented as Paper 255 at the 45th AIAA Aerospace Sciences Meeting and Exhibit, Reno, Nevada, 2007; received 21 February 2007; revision received 14 May 2007; accepted for publication 17 June 2007. Copyright © 2007 by The Boeing Company. Published by the American Institute of Aeronautics and Astronautics, Inc., with permission. Copies of this paper may be made for personal or internal use, on condition that the copier pay the $10.00 per-copy fee to the Copyright Clearance Center, Inc., 222 Rosewood Drive, Danvers, MA 01923; include the code 0021-8669/08 $10.00 in correspondence with the CCC.

*Boeing Technical Fellow, Enabling Technology and Research. Associate Fellow AIAA.
†Boeing Technical Fellow, Enabling Technology and Research. Senior Member AIAA.
‡Technical Specialist, Flight Sciences. Member AIAA.
§Boeing Technical Fellow, Flight Sciences. Associate Fellow AIAA.

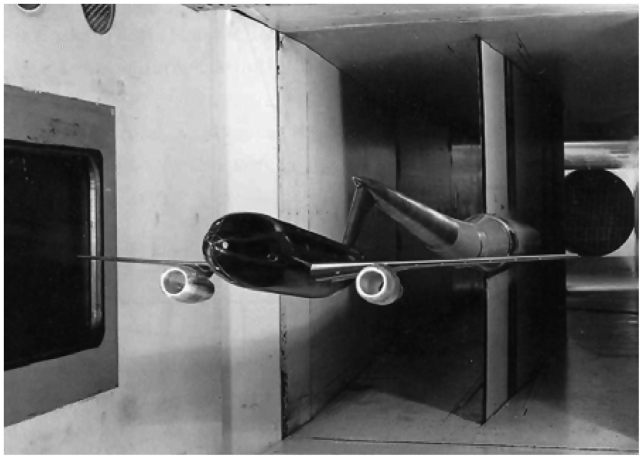

Fig. 1 DLR-F6 wing-body-pylon-nacelle model.

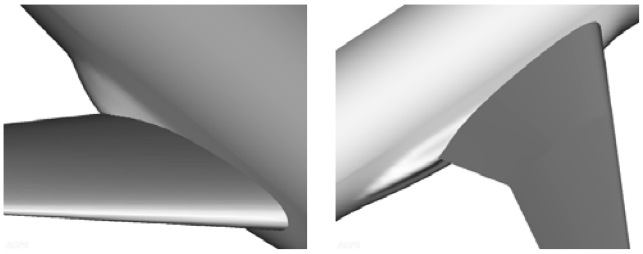

Fig. 2 FX2B wing-body fairing.

subject of a future wind-tunnel test. The planned Reynolds number (based on mean aerodynamic chord) is 5×10^6.

III. CFD Methods

The focus of the third AIAA DPW was the use of Navier–Stokes solvers to predict aerodynamic drag. These solvers can be characterized by the type of grid structure (structured, unstructured, or overset) they use. Some solvers can use more than one type of grid structure. This paper reports on the use of structured and unstructured solvers. A companion paper reports on the use of overset solutions [12].

A. Structured Solver: Zeus/CFL3D

Product development engineers must be able to focus on engineering processes: they have little time for manipulating CFD "processes." In other words, codes must be very user oriented. Stable "productionized," packaged software solutions enable and promote consistent processes. These solutions not only put CFD into the hands of the product development and product support engineers, they also allow the "expert" user to get fast results with reduced variation. These integrated, packaged software solutions combine the various CFD components to go from "lofts to plots" in a time scale consistent with a fast-paced engineering program.

A structured Navier–Stokes code is the heart of the Zeus system. The Zeus analysis system, illustrated in Fig. 3, is a series of UNIX shell scripts that coordinate surface grid generation, field grid generation, analysis, and postprocessing for structured grid Navier–Stokes CFD codes, such as CFL3D and TLNS3D. This system was developed with the goal of rapidly deploying CFD advancements to the user community. For a given type of configuration, a specific grid-generation process is developed and packaged into the system. To analyze a configuration using the ZEUS analysis system, users are only required to input geometry lofts and flow conditions: the system takes care of the rest of the analysis processes. The output from the system includes automatic plots of sectional data, convergence history, configuration force, and moment information, together with detailed flowfield files for flow visualization and diagnosis.

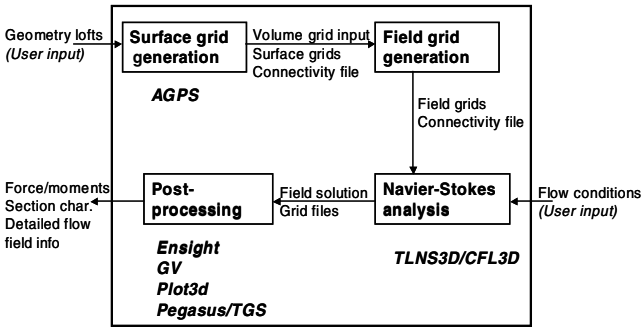

Fig. 3 ZEUS Navier–Stokes analysis system.

Although restricted to specific topologies, current configurations supported by ZEUS include commercial-type, transport-isolated nacelles, wing/body, wing/body/pylon/nacelle with either twin- or four-engine flowthrough or powered nacelles, and a wing/body/pylon/nacelle/horizontal–vertical tail. Options to support winglets and raked tips are also available. Configurations not included in the "standard" system can still be analyzed, but they will not benefit from the same degree of automation.

Of the two structured, multiblock Navier–Stokes solvers available within ZEUS, only CFL3D was used. CFL3D originated from the NASA Langley Research Center [13]. Reynolds-averaged Navier–Stokes (RANS) equations are solved using Roe's upwind scheme. A finite volume method is employed to construct both viscous and inviscid fluxes, and a multigrid scheme is used to accelerate convergence rate. Version 6.0 of the CFL3D code, with a message-passing interface (MPI) option suitable for a large-node parallel machine, was chosen for this study. Because of the use of a higher order upwind scheme in the CFL3D code, this option requires a high-quality Navier–Stokes grid to obtain a reliable converged solution. The code was originally developed with the thin-layer approximation, but it has since been extended to include the full Navier–Stokes terms.

B. Unstructured Grid Solver: BCFD

The BCFD code [14], developed at The Boeing Company, is a general purpose, implicit, multizone Euler and Navier–Stokes solver. It operates with any valid grids (structured and unstructured). BCFD has a mature library of boundary condition routines, available on a point-by-point basis. The Navier–Stokes equations are solved in thin layer or full formulation using Roe, HLLE (Harten–Lax–van Leer–Einfeldt), and Rusanov algorithms. The governing equations are discretized using the cell-centered, finite volume method. For steady-state flows, variable time steps based on local eigenvalues and a multigrid scheme are employed to speed convergence. For time-accurate calculations, BCFD uses a second-order, global Newton/dual-time algorithm, which provides second-order accurate updates in the physical-time domain across all zones.

BCFD dynamically allocates memory on a zonal basis, thereby minimizing computer hardware requirements. Distributed parallel processing is available using parallel virtual machine (PVM) and MPI message-passing protocols. A keyword input interface and extensive defaults simplify BCFD operation. Most BCFD options may be controlled zonally, allowing the user to balance the accuracy and cost of each solution [12].

C. Unstructured Grid Solver: CFD + +

CFD + + is a commercially available, general purpose code [15] used to solve the compressible Navier–Stokes equations. It allows the use of mixed element and overset grids. In this study, we used the mixed-elements option. The same set of unstructured grids generated by MADCAP/AFLR (modular aerodynamic computational analysis process/advancing front/local reconnection) for BCFD, consisting of a mixture of tetrahedra, prisms, and pyramids, was used. CFD + + allows a variety of turbulence models to be used, although only the Spalart–Allmaras (SA) turbulence model was used in this study. The discretization is a second-order, accurate, finite volume method, with

limiting to enable discontinuities to be captured without oscillations. The solver consists of an implicit method, which uses a semicoarsened multigrid algorithm with adaptive control of the time step to allow the solution to overcome difficulties in the transient phase.

D. Turbulence Models

Two turbulence models were used in these studies: Menter's two-equation shear-stress-transport (SST) model [16] and the SA turbulence model [17]. The SA model is a transport equation model for turbulent viscosity, which is calibrated on 2-D mixing layers, wakes, and flat plate boundary layers. It is local, compatible with any grid structure, and provides for user-specified laminar regions and trips.

IV. Grid Generation

To analyze a complex airplane configuration, the first step is to prepare or obtain a well-defined geometry loft for each configuration component. A well-defined geometry should have smooth physical coordinates, slope, and curvature variations in parameter space such that intersection curves between each component can be easily and accurately determined. The components are then combined to produce a watertight definition of the complete configuration.

A. Zeus Structured-Grid Generation

The provided initial graphics exchange specification (IGES) geometry files were imported into the Boeing Aerodynamics Grid and Paneling System (AGPS) [18], where the geometry was cleaned up and used to create watertight surface lofts.

The F6 wing-body configurations fit a class of configurations available from the ZEUS library, but they required a very minor modification (3–4 h) in the wing surface grid to account for the lack of a wing-body fairing in one case and the particulars of the FX2B fairing in the other.

An H-H grid topology was applied to the wing fuselage, one block going above the wing and upper fuselage and the other block going below the wing and lower fuselage, with the H grid stretching in the streamwise direction I, from upstream, covering the upper and lower wing fuselage, respectively, and then downstream. The second direction J is normal to the wing fuselage. Another H grid stretches in the wing spanwise direction K from the symmetry plane to the wing tip and then to the far field. For the wing with blunt trailing edge, an additional block with H-H grid is inserted between the upper and lower wing trailing edge wakes and behind the blunt wing trailing edge. It is degenerated onto the fuselage and onto the wing tip wake. A typical K-plane grid is illustrated in Fig. 4.

Within the Zeus system, command files for accessing and executing the AGPS are then used to generate surface grids for this topology. The resulting surface grid is watertight, with one-to-one point-matched blocks. The surface grid around the trailing edge of the wing-body configuration is shown in Fig. 5.

The Zeus system automatically prepares the block connectivity file that is essential for the volume grid generation and flow solver. The field grids are generated block by block using an advancing front method, which has been refined and enhanced over the years [19]. This procedure produces the viscous grids with desired y^+, grid-stretching ratio, and number of points inside of the boundary layer.

Although only three grids were called for in the drag convergence study, four sets of grids were generated for the grid refinement study of the two F6 configurations. Grids were refined by approximately 1.5 in each direction, while retaining at least three multigridable levels. This refinement resulted in grids of approximately 2.6×10^6, 9.2×10^6, 18×10^6, and 31×10^6 cells. These grids are labeled coarse, medium, medium fine, and fine, respectively. The medium grid is typical of the standard Zeus grid for a wing-body configuration. At each grid size, the total number and grid distribution for the two wing-body configurations are identical. The grids are available online via the DPW3 Web site [10]. A summary of the grid sizes is given in Fig. 6.

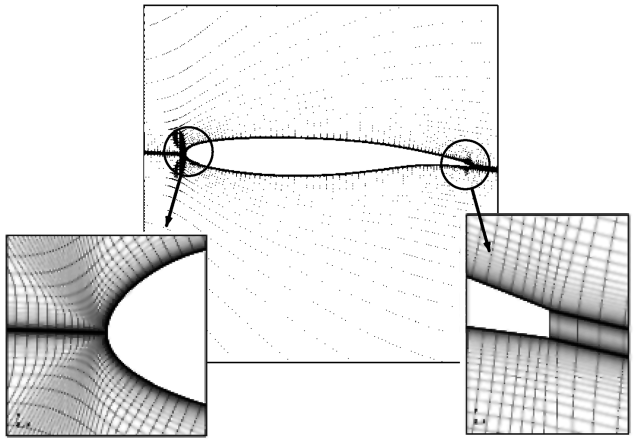

Fig. 4 Typical F6 wing grid topology (K plane).

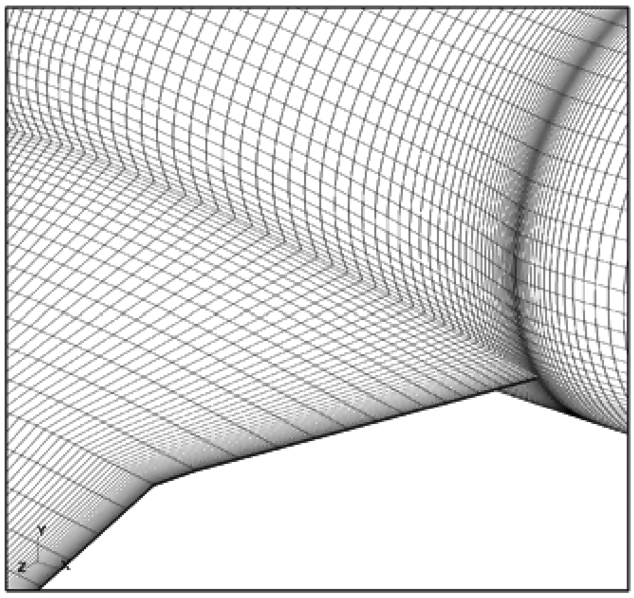

Fig. 5 Wing-body surface grid (coarse grid).

B. Unstructured Grid Generation

As in all grid-generation processes, the first step is to obtain a watertight definition of the geometry. The IGES files were prepared with CADfix [20] to obtain the watertight definition and then imported into MADCAP, a grid-generation package developed at Boeing that is capable of unstructured and structured grid generation. Much of the process is automated, with the user able to specify grid spacings on the surfaces, at which point MADCAP is able to autogrid the geometry. With the numerous grid spacing requirements for DPW3, a full autogrid was not possible. The grid consisted of triangles on the surface, except for the leading edge, which consisted of stretched quad elements. The guidelines set forth by DPW3 for the grid-generation requirements were closely followed.

Once the surface grid is defined, which includes the freestream, symmetry, and outflow boundaries, it is exported to AFLR [21], which is used to generate the volume grid. Prisms are used in the boundary layer, after which the grid transitions to tetrahedra. Boundary conditions are then specified, and the grid is split into multiple zones for parallel processing. Figures 7 and 8 display the surface grid for the coarse grid F6 case. Note the prisms in the boundary layer, which transition to tetrahedra.

The grid sizes are as follows: 3.8×10^6, 8.7×10^6, and 33.8×10^6 cells for the coarse, medium, and fine F6 grids, respectively, and 3.9×10^6, 7.8×10^6, and 35.8×10^6 cells for the coarse, medium, and fine F6 + FX2B grids, respectively. The grids are available online from the DPW3 Web site [10]. These grids were used for both

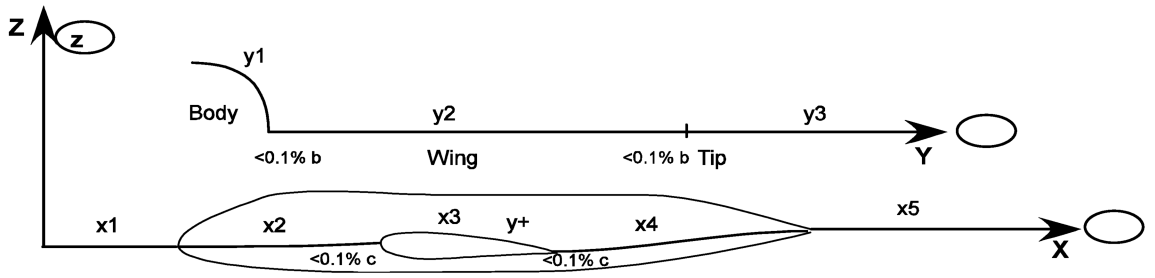

	x1	x2	x3	x4	x5	y1	y2	y3	z
Course	16	48	80	56	16	24	48	16	56
Med	24	72	120	88	24	32	72	24	84
Medfine	28	92	156	112	32	36	92	28	104
Fine	32	108	180	136	36	56	112	32	128

Blunt TE	z	y2
Course	32	48
Med	48	72
Medfine	60	92
Fine	72	112

Boundary Layer	# Cells	Ave y+
Course	24	0.82
Med	32	0.60
Medfine	40	0.50
Fine	48	0.40

Total Grid Size
2.6E+06
9.2E+06
1.8E+07
3.1E+07

Fig. 6 Structured grids.

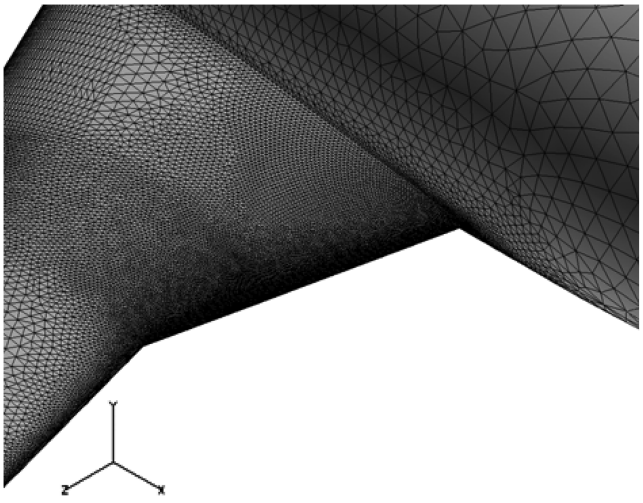

Fig. 7 Surface grid at wing root for F6 geometry.

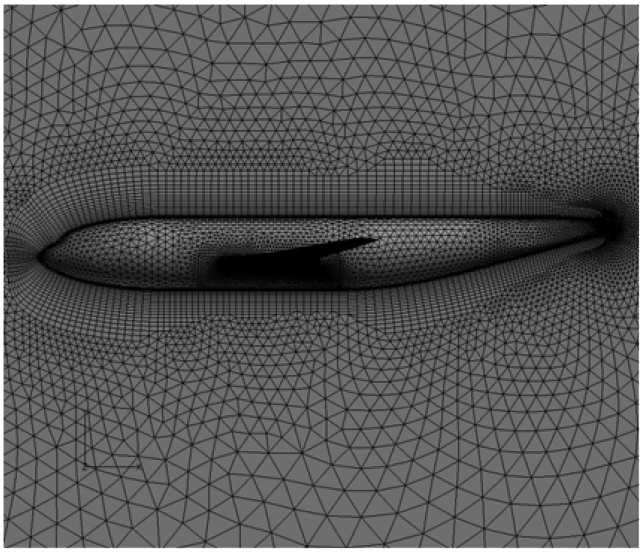

Fig. 8 Surface grid and reflection plane for F6 geometry.

the BCFD and CFD + + solutions. The wing-alone (DPW case 2) study was not performed in either code.

V. Structured Grid Results

The third AIAA DPW called for a drag convergence study, determination of the size of the side-of-body separation bubble, and the calculation of a drag polar for the F6 wing-body configurations.

The existence of wind-tunnel test data [10] for the basic DLR-F6 wing-body configuration from the second AIAA DPW suggested that an initial check of solution quality could be made by comparison to that data. The test data were acquired in the ONERA S2M wind tunnel, at a Reynolds number of 3×10^6 based on the mean aerodynamic chord. The specified Reynolds number for the third AIAA DPW calculations is 5×10^6 in anticipation of acquiring new wind-tunnel test data at that value. Solutions at 3×10^6 and 5×10^6 Reynolds numbers were computed using the medium grid. A comparison of wing pressures from these results with test data is shown in Fig. 9. The comparison is made at a fixed angle of attack, $\alpha = 0.50$ deg, matching that of the experimental data ($\alpha = 0.49$). Increasing Reynolds number has little visible effect on the solution, resulting in a slight aft movement of the shock wave. Overall agreement with the test data is excellent.

A series of solutions were obtained to investigate the influence of grid refinement on the predicted drag characteristics of the two wing-body configurations. Solutions were obtained at a constant lift coefficient, $C_L = 0.50$, using the four available grids with the following:

1) CFL3D with thin-layer Navier–Stokes terms using the SST turbulence model.

2) CFL3D with thin-layer Navier–Stokes terms using the SA turbulence model.

3) CFL3D with the full Navier–Stokes terms using the SST turbulence model.

4) CFL3D with the full Navier–Stokes terms using the SA turbulence model.

Multigrid and grid sequencing were used to accelerate solution convergence. In addition to monitoring residual reduction, drag and lift variation with iteration was monitored. Solutions were converged to $C_L = 0.5 + / - 0.0001$, with drag varying less than 0.05 count over the last 400 iterations, except for some coarse grid cases where drag settled into a steady oscillation of $+/ - 0.1$ counts or less.

Wing pressure distributions from the four grids on the baseline DLR-F6 wing-body using the SST turbulence model and the thin-layer approximation are shown in Fig. 10. With the exception of the

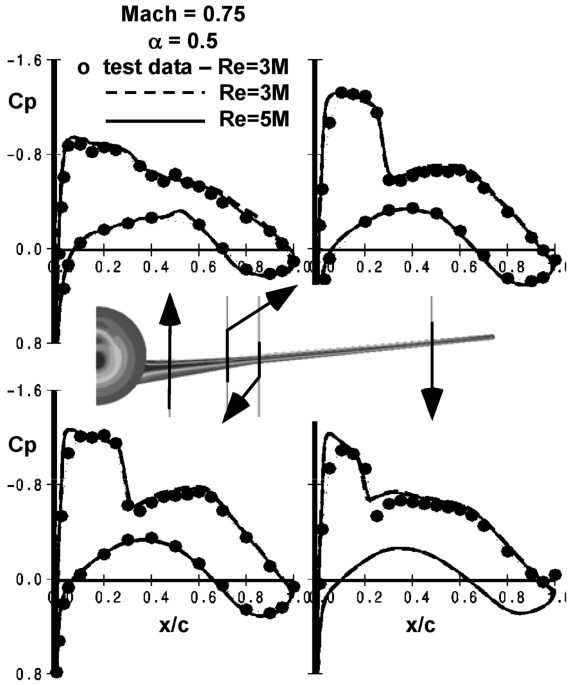

Fig. 9 Comparison of wing pressures with wind-tunnel data.

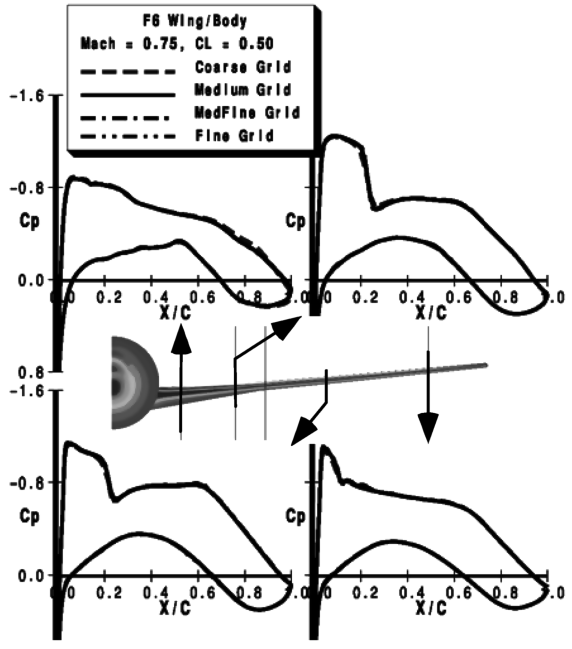

Fig. 10 Grid-size effects on wing pressure distribution.

coarse grid solution, the distributions are indistinguishable. This was typical of both configurations, the turbulence models, and the thin-layer and full Navier–Stokes approximations. For a fixed angle of attack, the shock location was slightly farther aft for the SA turbulence model compared to the SST model. Pressure distribution comparisons between the baseline F6 and the configuration with the FX2B fairing are shown in Fig. 11. Wing pressure distribution differences are pretty much confined close to the side of the body.

The objective of the FX2B fairing was to eliminate the side-of-body flow separation that is present on the basic DLR-F6 wing-body configuration. This was successfully achieved with a resultant drag reduction. The size of the side-of-body separation bubble plays a significant role in the drag of the basic wing-body configuration and therefore will impact the incremental drag increment due to the "cleanup" with the FX2B fairing. An oil-flow picture from the

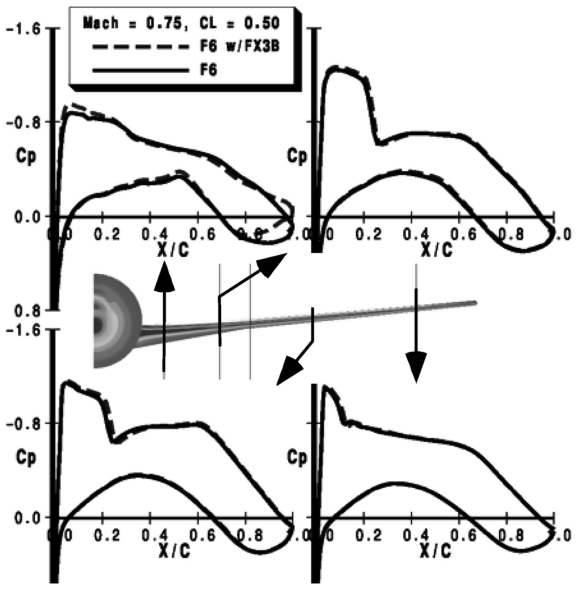

Fig. 11 Effect of FX2B fairing on wing pressures.

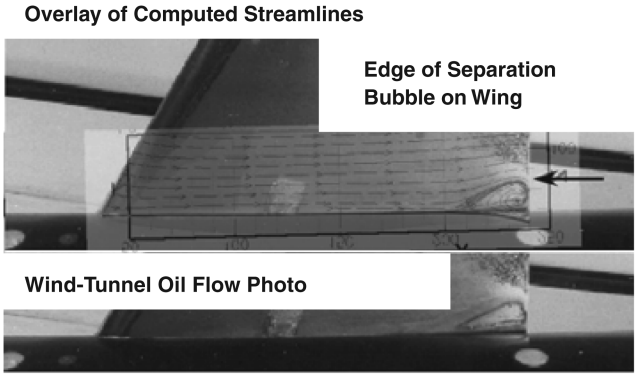

Fig. 12 Side-of-body flow separation.

ONERA wind-tunnel test at 3×10^6 Reynolds number is shown in Fig. 12. Overlaid on this picture are streamlines from a CFL3D thin-layer solution using the SST turbulence model at 5×10^6 Reynolds number. The computed streamlines are seen to be in reasonable agreement with the oil flow. A solution of the medium grid at 3×10^6 Reynolds number produced a separation bubble only 1.5 mm wider. The resolution of the overlay is no better than that.

Figure 13 shows a measure of the spanwise extent of the side-of-body separation bubble from solutions from CFL3D with thin-layer Navier–Stokes terms using the SA and SST turbulence models for the four grids. The values are plotted as a function of (GRIDFAC) $1/N^{2/3}$, where N is the total number of grid cells in the solution. A value of 0 would correspond to infinite grid size. The size of the separation bubble varies little for the three largest grid sizes. The use of the SA turbulence model resulted in a separation bubble slightly smaller than with the SST turbulence model. Use of the full Navier–Stokes terms resulted in separation bubbles 2–3 mm wider. Note that the extent of the separation did not encroach on the first row of pressure taps on the wing. This was also evident in the pressure distributions shown in Fig. 9.

Drag results from CFL3D with thin-layer Navier–Stokes terms using the SA and SST turbulence models are shown in Figs. 14 and 15, respectively. Drag is shown for both the basic F6 wing-body configuration and for the configuration with the FX2B fairing. Total drag is plotted as a function of (GRIDFAC) $1/N^{2/3}$, where N is the total number of grid cells in the solution. For a second-order accurate method, results from successively refined grids should form a straight line extrapolation to an infinite grid size. In actuality, successively refining grids by doubling them in every direction in 3-D

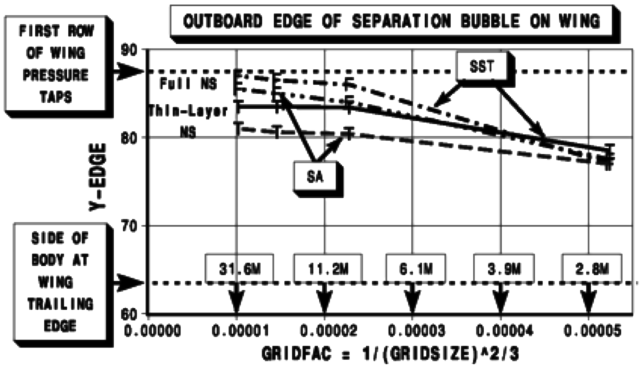

Fig. 13 Extent of separation bubble with CFL3D.

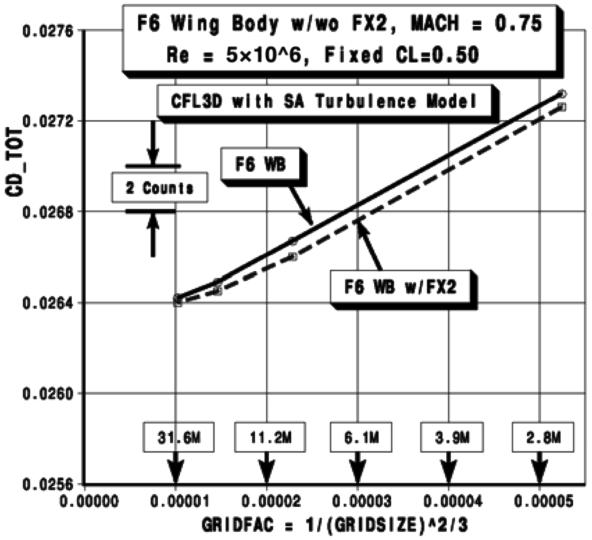

Fig. 14 Drag convergence for thin-layer CFL3D with the SA turbulence model; $C_L = 0.50, M = 0.75$.

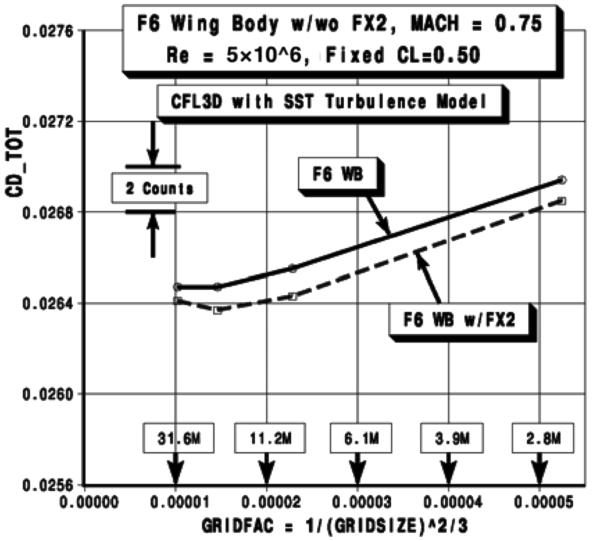

Fig. 15 Drag convergence for thin-layer CFL3D with the SST turbulence model; $C_L = 0.50, M = 0.75$.

for complex configurations is still not vary practical, although we believe that this set of grids is a reasonable approximation. As previously stated the solutions were converged until the drag varied by less than 0.05 counts over the last 400 iterations. However, as is typical of most Navier–Stokes codes it was not possible to drive the

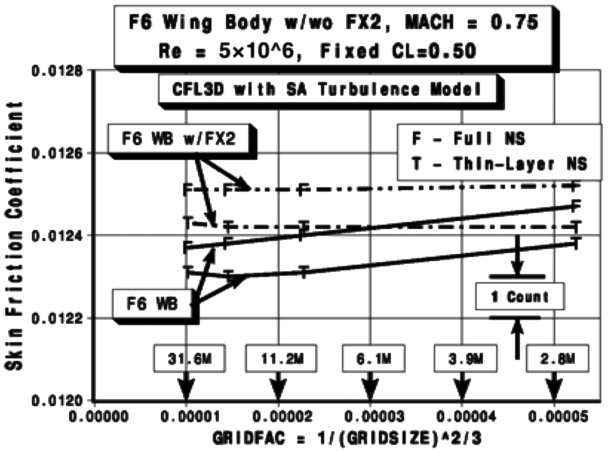

Fig. 16 Skin friction drag convergence for CFL3D with the SA turbulence model; $C_L = 0.50, M = 0.75$.

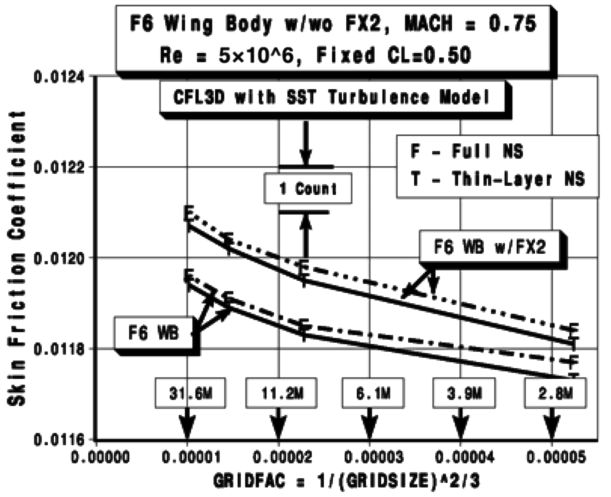

Fig. 17 Skin friction drag convergence for CFL3D with the SST turbulence model; $C_L = 0.50, M = 0.75$.

residuals to machine zero. It is interesting to note that while using the SA model results in a more linear variation of drag with grid size, it also results in a greater variation of the absolute value of drag with grid size. The lack of linearity of the drag convergence using the SST model is puzzling, particularly on the configuration with the FX2B fairing. On this configuration the flow is everywhere attached, and the significant flow features have been resolved. As will be seen in Fig. 17 it is the skin friction that continues to change with grid refinement. Solutions using CFL3D with the full Navier–Stokes terms were of similar character.

Total drag is made up of pressure drag plus skin friction drag. The pressure drag characteristics of the solutions using either turbulence model are very similar, differing mainly in level. It is the convergence characteristics of the skin friction drag that is most different, as shown in Figs. 16 and 17. Skin friction drag with the SA turbulence model shows little variation with grid size. Essentially no variation is shown for the configuration with the FX2B fairing, which exhibits no flow separation. With the SST model the levels of skin friction for both configurations continue to change with grid refinement. This appears to be the cause of the lack of linearity of total drag with grid refinement. The skin friction levels from the full Navier–Stokes solutions are similar to the thin-layer levels for the SST turbulence model but a count or so higher for the SA turbulence model. We do not have an explanation for these differences.

What about the absolute drag value? Do we believe that these CFD results indicate we can predict an absolute drag value for an infinite grid? Prediction may be possible with the SA model but not with the

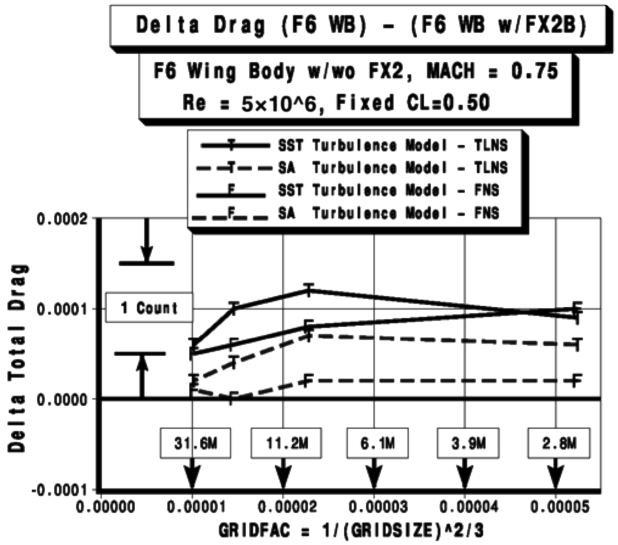

Fig. 18 Drag increment between configurations $C_L = 0.50$ and $M = 0.75$ CFL3D results.

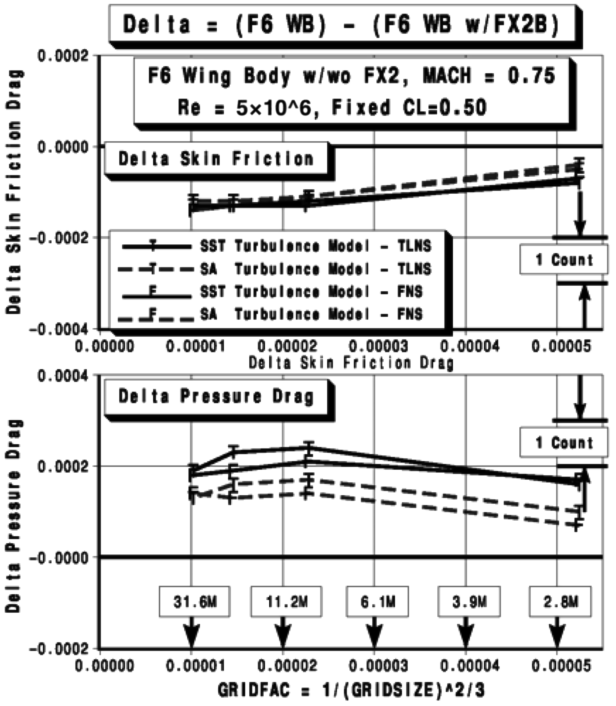

Fig. 19 Component drag increments for $C_L = 0.50$ and $M = 0.75$ CFL3D results.

SST turbulence model. Can the absolute value of drag be determined in a wind-tunnel test? Typical wind-tunnel corrections do not account for all the tare and interference effects in a test. The purpose of most wind-tunnel tests is not to produce absolute drag values but to produce *good incremental values* between configurations [7]. In a similar vein, can CFD produce good incremental values between configurations?

The incremental drag between the two configurations at a lift coefficient of $C_L = 0.50$ (basic F6 minus F6 with FX2B fairing) is shown in Fig. 18. Increments are from the two turbulence models, calculated using either the thin-layer or full Navier–Stokes approximation. Using the full Navier–Stokes terms in CFL3D yields a similar variation but only half the increment values compared to the thin-layer terms. What conclusions can be drawn from this figure?

1) Whichever turbulence model, thin layer or full approximation, is used, the incremental drag difference between the two configurations is very small—approximately one drag count or less.

2) The F6 wing body with the FX2B fairing has less drag.

3) The incremental values vary little for a wide range of grid sizes.

4) Extrapolating to infinite grid changes the sign of the increment.

Further insight is given by looking at the component increments shown in Fig. 19. The skin friction drag increment shows good convergence to the same value with increasing grid size. The configuration with the fairing has higher drag, which is consistent with the greater wetted area. The variation of the incremental drag is essentially due to the pressure drag, and this is where we see the biggest variation. The larger increment with the SST turbulence model is consistent with the larger size of the separation bubble in the basic configuration. The addition of the fairing eliminates the side-of-body separation, reducing the pressure drag at the expense of higher skin friction drag.

A series of solutions at different angles of attack were obtained for the two configurations using the medium grid, the thin-layer approximation, and the two turbulence models. Lift and pitching moment results for the two configurations show little difference. Using the SA turbulence model yields a slightly higher lift and slightly more negative pitching moment at a fixed angle of attack compared to the SST turbulence model. The incremental drag differences between the two configurations as a function of lift coefficient are shown in Fig. 20. Total and skin friction drag differences are shown for both turbulence models. As was indicated in the grid convergence study, at fixed lift, skin friction is greater with the fairing, and the difference in the skin friction increment between turbulence models is essentially nil. Below a lift coefficient of 0.55 to 0.60 the lower drag of the configuration with the fairing is due to lower pressure drag, and this increment is sensitive to the choice of turbulence model.

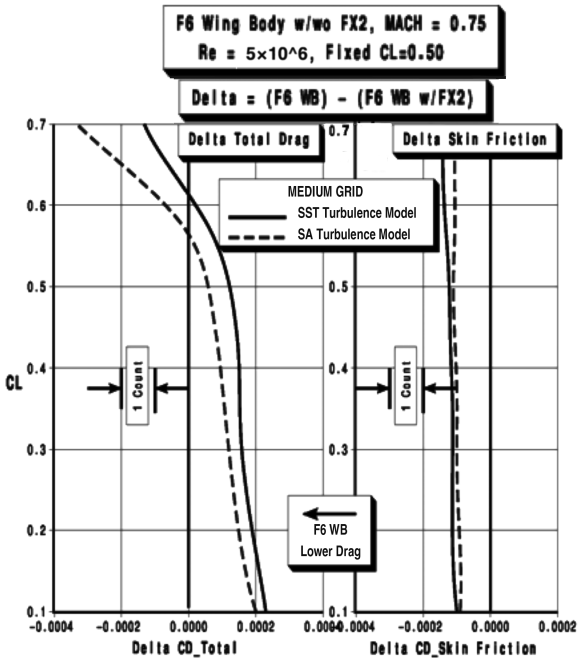

Fig. 20 Incremental drag vs lift coefficient for thin-layer CFL3D.

Based on these results (and a lot of other history) we choose to take the pragmatic view that we will rely on the incremental drag values. The values vary little over a wide range of grid size and appear to be reasonable. Extrapolating to infinite grid size is neither practical nor believable. The size of the drag increment and the differences between the two turbulence models would make it very difficult to resolve which is superior on the basis of this comparison alone. That said, experience still dictates that it is imperative that, for making incremental drag comparisons, gridding be kept as consistent as possible between configurations. As with use of the wind tunnel, great care must be taken to minimize extraneous influences that are not relative to the differences being sought.

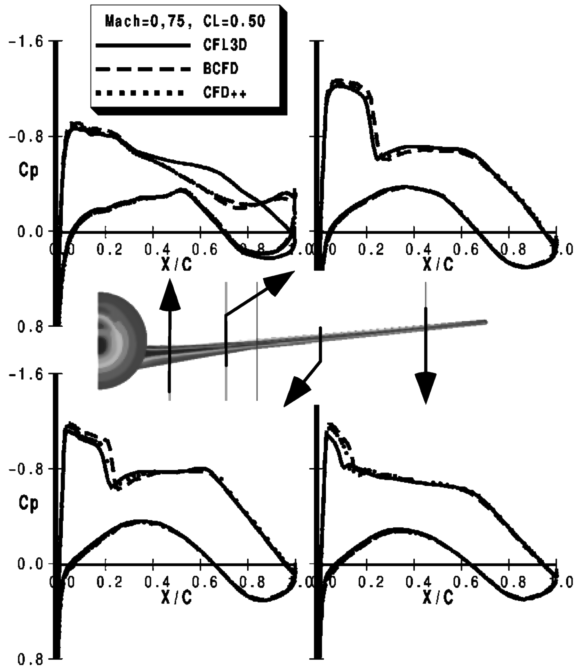

Fig. 21 Wing pressures on F6—CFL3D, BCFD, and CFD + +.

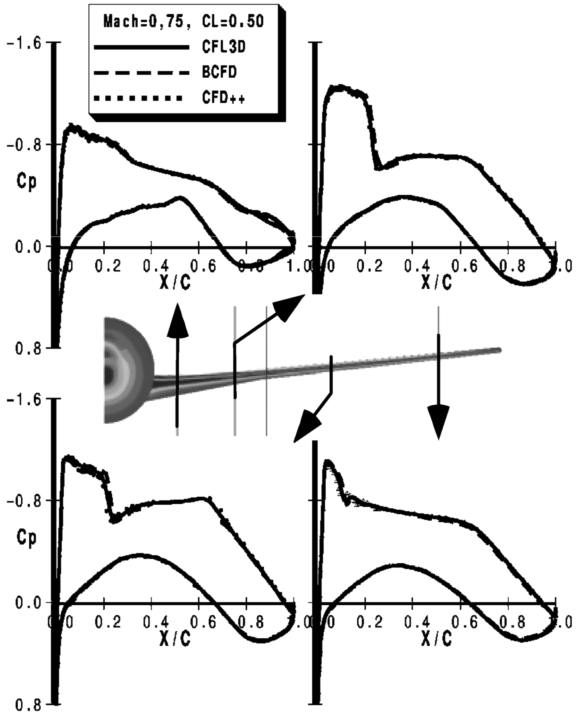

Fig. 22 Wing pressures on F6 with FX2B—CFL3D, BCFD, and CFD + +.

VI. Unstructured Grid Results

The application of unstructured grid Navier–Stokes solvers to transport type configurations at transonic speeds is new to us. Thus we do not have the many years of experience in unstructured grid generation and solution that should have been evident in the presentation of the structured results. The CFD results presented in this section were obtained using BCFD and CFD + +. The same grids were used in both codes. A full comparison between the F6 and F6 with FX2B configurations was performed using the SA turbulence model in both codes; a more limited comparison was performed in BCFD using the SST turbulence model due to unsteady effects from the side-of-body separation on the F6 configuration using the SST model, as well as limited time constraints. All solutions were run at $Re = 5 \times 10^6$, based on the mean aerodynamic chord of 141.2 mm. BCFD solutions were typically obtained in 24 h wall-clock time on a parallel-processing computer. In CFD + +, the finest grids were converged in about 200 node-hours and 1000 node-hours for the cases with and without the FX2B fairing, respectively, on an Opteron PC cluster. Convergence of over 7 orders of reduction of residual was achieved.

Solutions from the two unstructured grid codes were compared with the structured CFL3D results. All three codes were run with the SA turbulence model. Wing pressure distributions are shown for solutions at Mach = 0.75, $Re = 5 \times 10^6$, and a fixed $C_L = 0.50$. Results from the three codes for the F6 configuration are shown in Fig. 21. Note that the results from the two unstructured grid solutions are nearly identical and differ significantly from the CFL3D results at the inboard most station, $y = 87$ mm. The differences at the other stations are a result of matching C_L. The results of unstructured codes are at a slightly higher angle of attack to make up for the lift loss relative to CFL3D at the inboard most part of the wing. The lift loss shown at the inboard most station in Fig. 21 is a result of a much larger separation bubble relative to CFL3D solutions and the experimental data obtained at a lower Reynolds number. Similar results for the F6 with the FX2B fairing are shown in Fig. 22. Here the results from all three codes are much closer. Results from the unstructured codes are nearly identical with minor differences with the CFL3D results at the inboard most station.

BCFD was used to look at the effect of the turbulence model on the pressure distribution shown in Fig. 23. The figure shows a comparison between the F6 with FX2B geometry for both the SA and SST models. With the SST model, the shock on the upper surface moves slightly aft at a fixed lift coefficient. (Note: this result is consistent with the shock moving aft with the SA model at a fixed angle of attack.) The data shown are at $Y = 241$ mm; other locations are similar and are therefore not shown. Pressures on the lower side of the wing match very well between the two turbulence models.

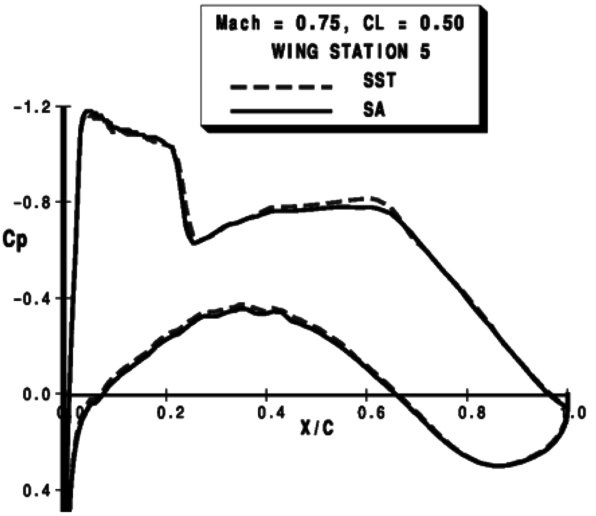

Fig. 23 Turbulence model effects on wing pressure distribution at $Y = 241$ mm for BCFD.

The separation bubble, as mentioned in the structured-grid results, is important to the resultant drag on the F6 configuration. A picture of the separation bubble is shown from the BCFD solution in Fig. 24 and from the CFD + + solution in Fig. 25. The pictures, which are very similar, show the fine-grid result in the wing-root region. It should be noted that these pictures were made with different postprocessing visualization codes and do not show the same perspective. The detail differences may not be meaningful given the differences in postprocessing, convergence characteristics of the two codes, and applicability of using a one-equation turbulence model in a steady RANS code to depict the unsteady flow phenomena inside the separation bubble. The external impact of the separation bubble may still be meaningful as indicated by the CFL3D results which

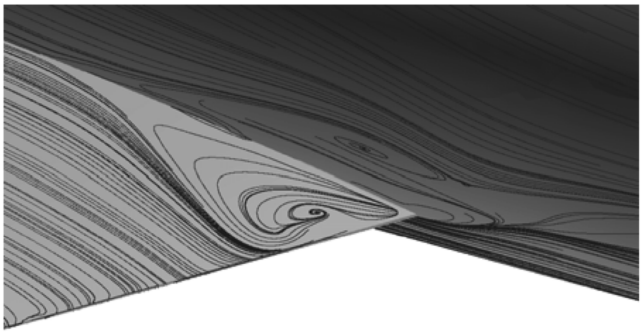

Fig. 24 Side-of-body separation predicted by BCFD.

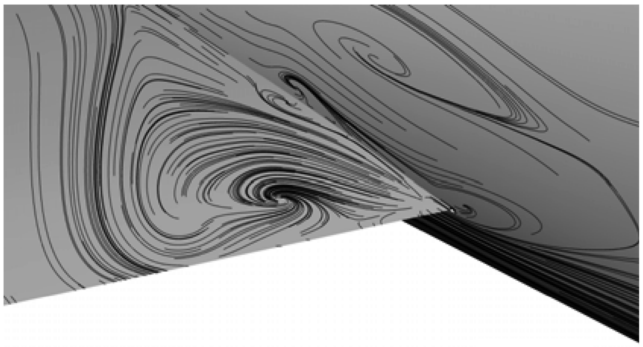

Fig. 25 Side-of-body separation predicted by CFD + +.

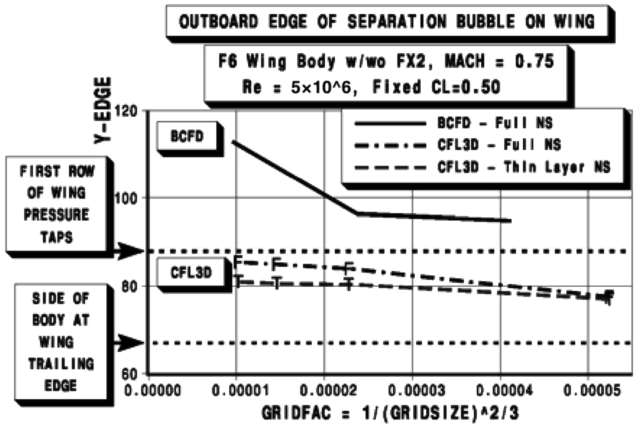

Fig. 26 Extent of separation bubble with fixed $C_L = 0.50$ predicted by BCFD.

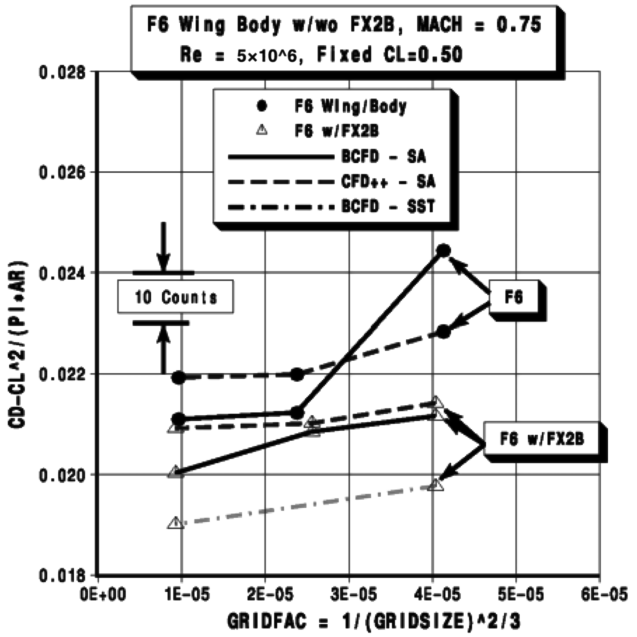

Fig. 27 Drag convergence with unstructured solvers BCFD and CFD + +.

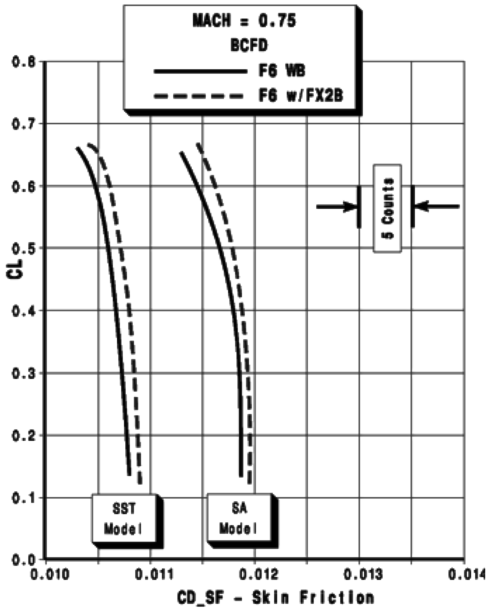

Fig. 28 Turbulence model effect on skin friction using BCFD.

closely matched the test data at a lower Reynolds number as indicated in Figs. 9 and 12. The extent of the separation bubble, as defined by the maximum buttline of the dividing surface streamline of the separation bubble, is seen to be larger from the unstructured grid solutions than the structured-grid results predicted. The extent of the separation bubble predicted by BCFD is shown in Fig. 26, which shows that the bubble is growing with increasing grid refinement. The size of the separation bubble predicted by CFD + + is essentially the same as predicted by BCFD. That trend is much more pronounced in the unstructured results compared to those of the structured CFL3D code. Also, for the unstructured grid codes the first row of pressure taps is within the separation bubble, as evident in earlier C_p plots in Fig. 21 that compared distributions from the three codes. The larger bubble results in significantly different pressure distributions at the inboard most wing station. Further work is necessary to understand to what extent these differences are due to code and/or grid type.

Drag results are the primary focus of the DPW3. Grid convergence plots at a fixed $C_L = 0.5$ are shown in Fig. 27. Results with the SA model with both unstructured codes are shown for the F6 and F6 with FX2B, and from the SST model in BCFD for the F6 with FX2B. A grid convergence study was not performed on the F6 with the SST model. The trends observed in Fig. 27 show a reduction in drag with the addition of the FX2B fairing and a somewhat lower drag using the SST model compared to the SA turbulence model. These trends are not unlike those seen with the structured code.

To isolate the differences seen due to the turbulence model effect, Fig. 28 displays the behavior of the skin friction as we vary lift. It can be seen that the majority of the increment due to the turbulence model seen in the drag shown in Fig. 27 can be attributed to the skin friction. The skin friction is consistently lower for the SST model, regardless of geometry. Also note that the skin friction is slightly higher for the F6 with FX2B case, as the wetted area is larger after the inclusion of the fairing.

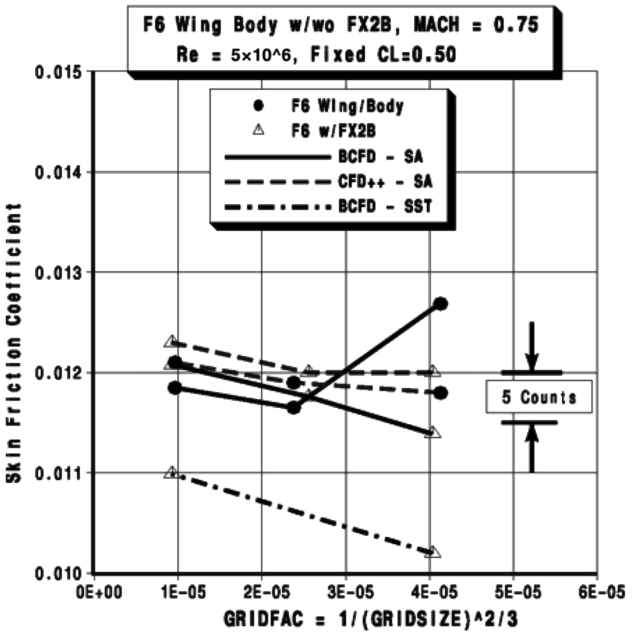

Fig. 29 Skin friction drag convergence using BCFD.

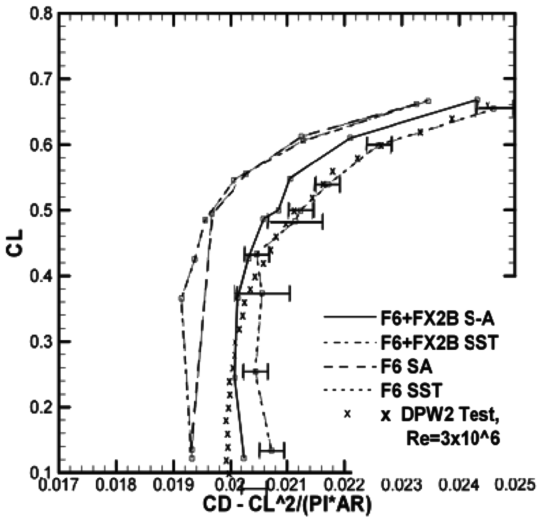

Fig. 30 Drag polar for BCFD unstructured grid.

The grid convergence of the skin friction is shown in Fig. 29. The skin friction is seen to increase with increasing grid density. The high value of drag for the coarse grid BCFD solution is seen to be due to the corresponding high value of skin friction from that solution. Whether this high value is due to a convergence problem in the coarse grid solution is not known. It is seen that the infinite grid skin friction extrapolation would differ by approximately 10 counts for the F6 with FX2B geometry when comparing the SA and SST turbulence model, with the SST model having the lesser drag. This is a much greater difference than indicated by the CFL3D solutions shown in Fig. 17.

A drag polar for the two configurations, shown in Fig. 30, was computed in BCFD on the medium grid for each configuration. We looked at the SA and SST models for both the F6 and F6 with FX2B and compared the results with the DPW2 experimental data, which were identical to the F6 geometry but at $Re = 3 \times 10^6$ based on mean aerodynamic chord. The SA model is seen to closely match the DPW2 data for the F6 case. We can also see that the effect of the SST model is a reduction in drag for either geometry. Note the error bars on the F6 geometry with the SA model: these bars represent the magnitude of the drag oscillations in the solution history and quantify the effect the side-of-body separation has on the solution. Because of these oscillations, only a limited number of SST solutions were performed with the F6 geometry. Also note that the drag polar shape is not sensitive to the turbulence model.

The incremental drag difference between the two configurations predicted by the three codes using the SA turbulence model is summarized in Fig. 31. Also shown is the extent of the separation bubble predicted by the codes. The extent of the separation bubble and the incremental drag predicted by the unstructured codes is much larger than predicted by CFL3D. A wind-tunnel test is planned for summer 2007 which should confirm the magnitude of the drag increment between configurations and the extent of the separation bubble in the F6 configuration. The drag increment between the F6 and F6 with FX2B from either unstructured code does not exhibit linear convergence; each has a minima at the medium grid size. A reason for this could be the "family" of grids each unstructured grid belongs to. In this form of grid convergence plot, typically, nested structured grids are used, which will, by definition, all belong to the same grid family. However, this is not the case for advancing front method used to generate these unstructured grids. Each volume grid will have a different arrangement of prisms and tetrahedra, depending on how the advancing front method fills the volume. Even slight changes on the surface grid can cause noticeable changes in the volume grid. One way to possibly get around this would be to generate the volume grid in two pieces: one piece common to both the F6 and F6 with FX2B, and a second piece that isolates the fairing region. This approach minimizes the change in the volume grid between the two configurations; it should be looked at in further drag prediction studies on unstructured grids to minimize the scatter in the grid convergence plots.

VII. Conclusions

Previously published results [3,7] and many in-house studies have shown accurate prediction of drag increments between configurations. Accurate prediction is key to successful configuration design. The ability to predict incremental drag between known configurations is essential to drag-based multipoint design and optimization [3]. In those instances where drag increment prediction has been successful, the geometry and the test data were well known. The flow over the configurations was well behaved and exhibited no obvious separation. The F6 configuration of this study is a deceptively difficult case. Accurate prediction of difficult flow features is important, not only for drag prediction, but also for flight stability and control prediction issues. The experience in using structured-grid methods for the past 25+ years has been invaluable in establishing viable processes for effectively using these methods. As this study [8] shows, the absolute value of drag varies with grid size and turbulence model. It is neither practical nor necessarily even useful to try to do a drag convergence study on every configuration iteration during an airplane development program. What is essential for the effective use of CFD is the ability to predict drag increments between similar configurations. In this study, the structured code results demonstrated a consistent prediction of the drag increment within a few tenths of a count between the two configurations. The predicted drag increment using the structured ZEUS/CFL3D system between the two configurations is on the order of 1 drag count. A wind-tunnel test is planned for summer 2007 [8] which, it is hoped, will confirm the accuracy of the prediction.

The unstructured code(s) results indicate a need for further study, in "best practice" methods, of drag increment results. The experience base for using unstructured grid methods for transonic analysis of transport configurations does not yet exist (in this organization) at this time (2006). Because structured-grid methods have been adequate for analyzing these types of configurations, there has been no urgency in the past to adopt unstructured methods. However, with the increasing interest in including a wider range of configurations with more geometric complexity in the analysis, there is now an interest in exploiting the potential advantages of unstructured solvers. The unstructured results indicate that the analysis of the F6 geometry is deceptively difficult with a side-of-body separation

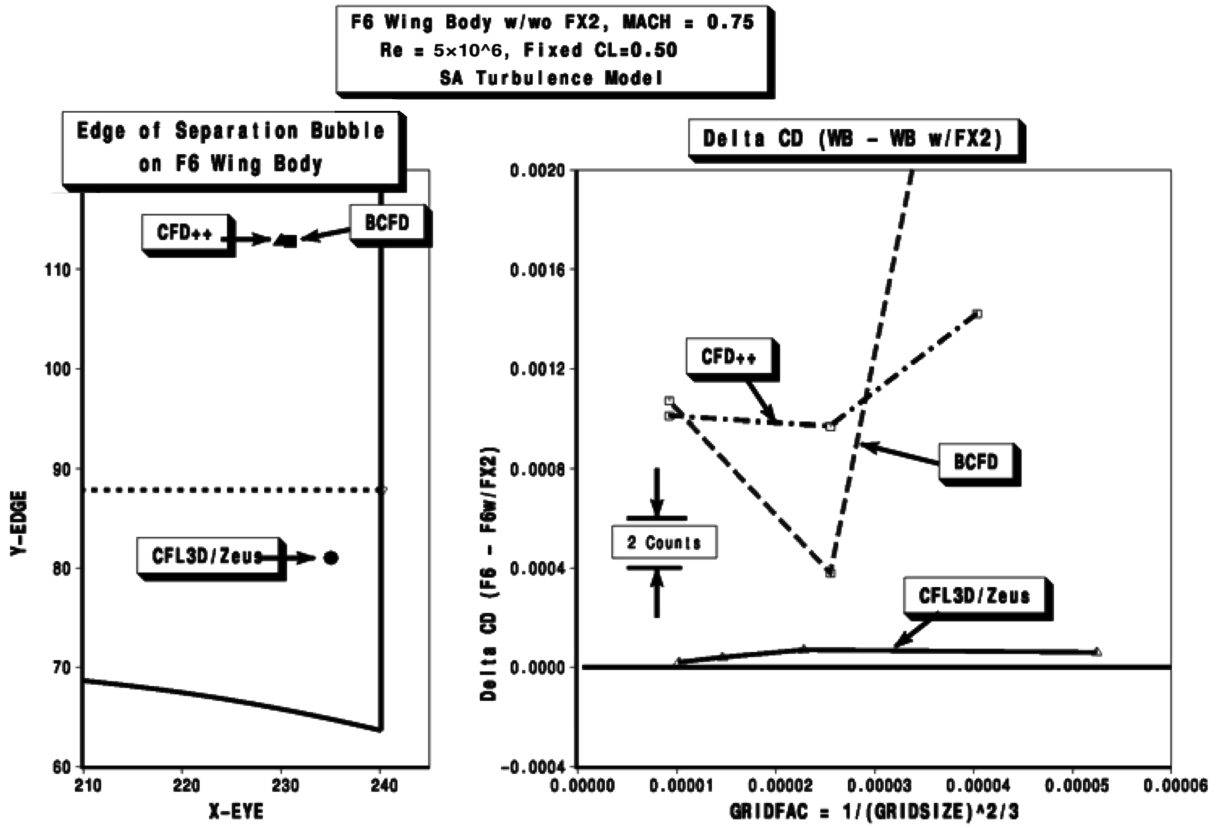

Fig. 31 Summary of incremental drag between the F6 with/without FX2B fairing as predicted by CFL3D, BCFD, and CFD + + using SA turbulence model.

bubble. The addition of the fairing, which eliminated the separation, noticeably increased solution stability and improved the convergence properties in both unstructured codes.

The present results indicate the status of the unstructured grid capabilities in CFD + + and BCFD (version 4.0) as of DPW3 in June of 2006. However, the state of the art in unstructured solvers is rapidly changing. In fact, it is expected that the drag predictions with unstructured codes will continue to be enhanced by the anticipated publication time of this journal article, as advancements in both numerics and grid generation are being made on a frequent basis. Preliminary results using BCFD (version 5.0) are indicating that the slope limiter of Venkatakrishnan [22] reduces drag in BCFD by 10+ counts for the DPW F6 configuration compared to the current slope limiting procedure employed in BCFD. The biggest issue still appears to be with the grid generation, not the two unstructured solvers. Unstructured grid-generation best practices are being established on an ongoing basis. We believe that, to predict accurate increments, as much of the unstructured volume grid as possible should be kept constant between the geometries. This practice is currently being investigated. As best practices are developed for use of the unstructured codes, these too will exhibit the same accuracy and reliability experienced with the structured codes.

Acknowledgments

The authors wish to acknowledge the contributions of N. Jong Yu, Tsong-Jhy Kao, Emanuel R Setiawan, Tsu-Yi Bernard Su, Senthan Swaminathan, Moeljo Hong, Andrew Cary, Andy Dorgan, Mark Fisher, and Metacomp Technologies. None of this work would have been possible without their considerable contributions. The authors also wish to acknowledge the use of the computers at the National Center for Computational Sciences (NCCS) at the Oak Ridge National Laboratory for some of the results used in this study.

References

[1] Rubbert, P. E., "AIAA Wright Brothers Lecture: CFD and the Changing World of Airplane Design," International Council of the Aeronautical Sciences Paper ICAS-94-0.2, Sept. 1994.

[2] Tinoco, E. N., "The Changing Role of Computational Fluid Dynamics in Aircraft Development," AIAA Paper 98-2512, June 1998.

[3] Johnson, F. T., Tinoco, E. N., and Yu, N. J., "Thirty Years of Development and Application of CFD at Boeing Commercial Airplanes, Seattle," AIAA Paper 2003-3439, June 2003.

[4] Pfeiffer, N. J., "The Use of CFD in the Design Process for Configuration Drag," AIAA Paper 2000-0380, Jan. 2000.

[5] Cosner, R. R., "Assessment of Vehicle Performance Predictions Using CFD," AIAA Paper 2000-0384, Jan. 2000.

[6] Tinoco, E., N., "An Assessment of CFD Prediction of Drag and Other Longitudinal Characteristics," AIAA Paper 2001-1002, Jan. 2001.

[7] Tinoco, E. N., and Bussoletti, J. E., "Minimizing CFD Uncertainty for Commercial Airplane Applications," AIAA Paper 2003-0407, Jan. 2003.

[8] Vassberg, J. D., Tinoco, E. N., Mani, M., Brodersen, O. P., Eisfeld, B., Wahls, R. A., Morrison, J. H., Zickuhr, T., Laflin, K. R., and Mavriplis, D. J., "Summary of the Third AIAA CFD Drag Prediction Workshop (Invited)," AIAA Paper 2007-0260, Jan. 2007.

[9] Morrison, J., and Hemsch, M., "Statistical Analysis of CFD Solutions from the Third AIAA Drag Prediction Workshop (Invited)," AIAA Paper 2007-0254, Jan. 2007.

[10] *3rd AIAA Drag Prediction Workshop*, http://aaac.larc.nasa.gov/tsab/cfdlarc/aiaa-dpw/.

[11] Vassberg, J. D., Sclafani, A., and DeHaan, M., "A Wing-Body Fairing Design for the DLR-F6 Model: A DPW-III Case Study," AIAA Paper 2005-4730, June 2005.

[12] Sclafani, A., Vassberg, J., Rumsey, C., and Mani, M., "Drag Prediction for DPW-III Wing-Body and Wing-Alone Cases Using OVERFLOW, CFL3D, and BCFD on an Overset Mesh," AIAA Paper 2007-0257, Jan. 2007.

[13] Biedron, R. T., and Rumsey, C. L., "CFL3D User's Manual," NASA TM-1998-208444, June 1998.

[14] Mani, M., Cary, A., and Ramakrishnan, S. V., "A Structured and Hybrid-Unstructured Grid Euler and Navier-Stokes Solver for General Geometry," AIAA Paper 2004-524, Jan. 2004.

[15] Chakravarthy, S., Palaniswamy, S., Goldberg, U., Peroomian, O., and Sekar, B., "A Unified-Grid Approach for Propulsion Applications," *AIAA/ASME/SAE/ASEE Joint Propulsion Conference*, AIAA, Reston, VA, July 1998.

[16] Menter, F. R., "Two-Equation Eddy-Viscosity Turbulence Models for Engineering Applications," *AIAA Journal*, Vol. 32, No. 8, Aug. 1994, pp. 1598–1605.

[17] Spalart, P. R., and Allmaras, S. R., "A One-Equation Turbulence Model for Aerodynamic Flows," AIAA Paper 92-0439, Jan. 1992.

[18] Capron, W. K., and Smit, K. L., "Advanced Aerodynamic Applications of an Interactive Geometry and Visualization System," AIAA Paper 91-0800, Jan. 1991.

[19] Su, T. Y., Wilkinson, W. M., and Yu, N. J., "Structured Navier-Stokes Grid Generations for Propulsion-Integrated Airplane Configurations," *5th International Conference on Numerical Grid Generation in Computational Field Simulations*, Mississippi State University, Starkville, MS, 1–5 April 1996.

[20] CADfix Product Overview, ITI TranscenData Interoperability Solutions for CAD/CAM/CAE/PLM, http://www.transcendata.com/products/cadfix/index.htm.

[21] Marcum, D. L., "Advancing-Front/Local-Reconnection (AFLR) Unstructured Grid Generation," *Computational Fluid Dynamics Review*, Vol. 1, edited by M. Hafez and K. Oshima, World Scientific, Singapore, 1998.

[22] Venkatakrishnan, V., "Convergence to Steady State Solutions of the Euler Equations on Unstructured Grids with Limiters," *Journal of Computational Physics*, Vol. 118, No. 1, 1995, pp. 120–130. doi:10.1006/jcph.1995.1084